Journal of Materials Chemistry B

ROYAL SOCIETY OF CHEMISTRY

PAPER

View Article Online
View Journal | View Issue

Cite this: J. Mater. Chem. B, 2023, 11, 6335

Construction of Fe-doped ZIF-8/DOX nanocomposites for ferroptosis strategy in the treatment of breast cancer†

Yuyu Zhong,‡[a] Zhaoxi Peng,‡[c] Yanqiong Peng,‡[b] Bo Li,*[c] Ying Pan,*[ab] Qin Ouyang,*[d] Hiroshi Sakiyama,[e] Mohd. Muddassir[f] and Jianqiang Liu*[ab]

Received 5th April 2023,
Accepted 31st May 2023

DOI: 10.1039/d3tb00749a

rsc.li/materials-b

Breast cancer has become one of the top five commonest causes of cancer death. The use of ferroptosis to induce the generation of reactive oxygen species (ROS) in cancer cells presents a promising and potential strategy for cancer treatment. Herein, a series of facile bimetallic nanoparticles (*x*% Fe-doped ZIF-8) were synthesized and tested, and doxorubicin (DOX), a classic drug for breast cancer therapy, was encapsulated. After comparing the ratios of $Fe^{2+}/(Fe^{2+} + Zn^{2+})$, 7% Fe-doped ZIF-8 (7FZ) was found to be the most suitable particle for medical application. The drug loading efficiency of DOX@7FZ was 58.01 ± 0.02%. The pH-sensitive DOX@7FZ was degraded and DOX was released in lysosomes once internalized. Both the intracellular content of iron and ROS increased significantly. Meanwhile, the cell viability declined to 13.98% in 24 h at a concentration of 60 μg mL^{-1} and the IC_{50} was 42.68 μg mL^{-1}. Moreover, the expression of Bcl-2 and GPX-4 proteins decreased in a time-dependent manner, indicating that DOX@7FZ was able to enhance the ROS level in cancer cells *via* a synergistic effect between apoptosis and ferroptosis. The mechanism of action of DOX@7FZ was further verified using hematoxylin and eosin staining and immunohistochemical staining of Bcl-2 and GPX-4. These remarkable characteristics of DOX@7FZ may inspire further advancements in the treatment of breast cancer.

1. Introduction

According to the latest data published by the International Agency for Research on Cancer (IARC), the number of cases of breast cancer is 2.26 million, surpassing 2.2 million cases of lung cancer.[1] Breast cancer has become the fifth commonest cause of cancer death. Chemotherapy has remained the mainstay of treatment for various stages of breast cancer.[2–4] However, chemotherapeutic drugs can cause side effects, leading to significant consequences in terms of treatment adherence and even patients' quality of life.[5] Thence, a combined chemotherapy strategy has been proposed, aiming to reduce the doses of drugs and realize a synergistic effect for effective treatment.[6]

Reactive oxygen species (ROS) play important roles in tumorigenesis.[7] The intracellular ROS include superoxide ion ($O_2^{\bullet -}$), hydrogen peroxide (H_2O_2), and hydroxyl radicals ($^{\cdot}OH$).[8,9] Having an important influence on the behavior of cancers and the stromal components of the tumor, ROS can regulate the development and survival of cancer cells. Thence, ROS can be both essential and lethal to tumor cells. Based on these, ROS-modulating therapies (photodynamic therapy, sonodynamic therapy, and chemodynamic therapy) have been proposed to disrupt either the intracellular or tumor microenvironment (TME) ROS.[10–12] Despite having the advantage of yielding ROS accurately in tumor sites, these therapies are still suffering from the lack of oxygen to generate abundant ROS effectively.

In contrast to apoptosis, autophagy, and necroptosis, ferroptosis is a non-apoptotic mode of cell death characterized by the accumulation of iron-dependent lipid peroxides (LPOs).[13–15] As Stockwell *et al.* described, there are three hallmarks of ferroptosis: the loss of LPO repair capacity of glutathione peroxidase-4 (GPX-4), the oxidation of polyunsaturated-fatty-acid-containing

[a] Key Laboratory of Research and Development of Natural Drugs, Guangdong Medical University Key Laboratory of Research and Development of New Medical Materials, and School of Pharmacy, Guangdong Medical University, Dongguan, 523808, China. E-mail: panying@gdmu.edu.cn
[b] The First Dongguan Affiliated Hospital, Guangdong Medical University, Dongguan, 523808, China. E-mail: jianqiangliu8@gdmu.edu.cn
[c] Department of Vascular Surgery, Shanghai Ninth People's Hospital, Shanghai Jiao Tong University School of Medicine, Shanghai, China. E-mail: boli@shsmu.edu.cn
[d] Department of General Surgery, Dalang Hospital, Dongguan, Guangdong, China. E-mail: ouyangqin8@sina.com
[e] Department of Science, Faculty of Science, Yamagata University, 1-4-12 Kojirakawa, Yamagata 990-8560, Japan
[f] Department of Chemistry, College of Sciences, King Saud University, Riyadh 11451, Saudi Arabia

† Electronic supplementary information (ESI) available. See DOI: https://doi.org/10.1039/d3tb00749a

‡ These authors contributed equally to this work and are joint first authors.

phospholipids (PUFA-PLs), and the availability of redox-active iron.[16] In ferroptosis, the labile iron, which should have stayed in ferritin in the form of Fe(III), is released to the labile iron pool to generate free radicals and mediate lipid peroxidation through the Fenton reaction.[17–19] As ferroptosis occurs, cells are exposed to large amounts of ROS, leading to cell death. Accumulating evidence indicates that ferroptosis plays a vital role in breast cancer and inducing ferroptosis in tumor cells is a promising anticancer strategy.[20]

Doxorubicin (DOX), a broad-spectrum anthracycline antibiotic, is one of the commonly used agents for breast cancer therapy.[21,22] Various molecular mechanisms have been used to explain how DOX intercalates into DNA, generates free radicals, and induces membrane lipid oxidation.[23] However, DOX also has toxic effects on normal cells, particularly resulting in irreversible cardiotoxicity.[24] Growing evidence suggests that DOX can increase the expression levels of calreticulin (CRT) on the surface of tumor cells to further stimulate the release of high mobility group box 1 (HMGB1).[25,26] To address the problem mentioned above, a good number of nanoparticles, for instance, liposomes, polymer micelles, and mesoporous silica nanoparticles, are designed to package and deliver DOX.[27–29]

A combination therapy based on ferroptosis and apoptosis in tumor cells is a promising way to treat tumors. There are three pathways for nanoparticles to induce ferroptosis: lysosomal dysfunction, membrane impairment, and mitochondrial damage.[30–34] Among these pathways, causing iron overload in cells is a simpler and direct method to induce mitochondrial damage and further mediate the process of ferroptosis. Metal-based nanoparticles, especially iron-based nanoparticles, are excellent candidates that affect iron homeostasis directly.[30] Zeolitic imidazolate framework-8 (ZIF-8), formed from the coordination of 2-methylimidazole (2-MIM) and Zn^{2+}, is a kind of metal-based porous material.[35,36] It has been widely used as a nanocarrier because of its several advantages, including high porosity, satisfactory biocompatibility, as well as acidic-responsive degradation.[37–42] Several studies have reported the successful synthesis of metal-doped ZIF-8 since 2014, and the majority of these studies were performed in the fields of nanocatalysis and gas storage while few studies were performed in medicine due to unclear toxicity produced by bimetallic nanoparticles.[43–47]

Inspired by this, a facile synthesized bimetallic ZIF-8 was presented and used as both a ferrous ion supplier and a drug carrier. Conveniently, DOX was encapsulated into bimetallic Fe-doped ZIF-8 in an appropriate ratio (7% Fe-doped ZIF-8, 7FZ) *via* a one-pot synthesis process. The obtained 7FZ retained the characteristic pH-responsive release and excellent biocompatibility of ZIF-8. Following the internalization of the nanoparticles (DOX@7FZ) in breast cancer cell line MCF-7 cells, acidic degradation of the nanoparticles facilitated the release of DOX and accumulation of ferrous ions. The released ferrous ions disrupted the intracellular iron balance *via* the Fenton reaction and increased the concentration of the ferrous ions, leading to oxidative stress-induced ferroptosis in MCF-7 cells. Moreover, the series of reactions mentioned above have improved DOX-induced apoptosis synchronously. As a result of the synergistic effect between apoptosis and ferroptosis, the oxidative stress induced in the MCF-7 cells increased significantly, leading to cell death (Scheme 1).

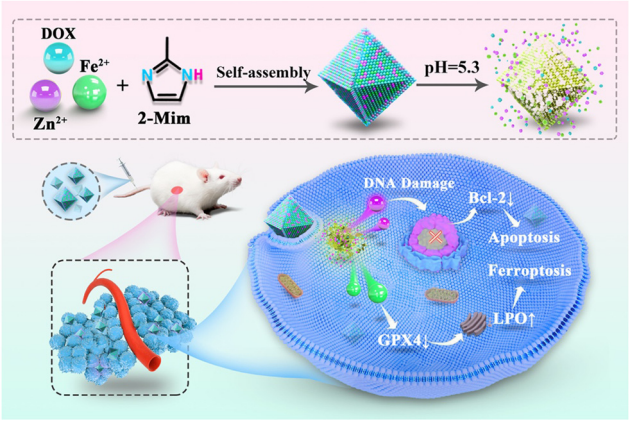

Scheme 1 The synthesized route to the nanoparticle DOX@7FZ and the proposed molecular mechanism for the DOX@7FZ-induced synergism between apoptosis and ferroptosis in tumor cells.

2. Materials and methods

2.1. Reagents

In this work, all the reagents and organic solvents were of analytical grade and they were utilized without further purification (Table S1, ESI†).

2.2. Synthesis and characterization of materials

The Fe-doped ZIF-8 was synthesized *via* a method reported before.[46] Both $Zn(NO_3)_2{\cdot}6H_2O$ and $FeSO_4{\cdot}7H_2O$ were added to 20 mL methanol; meanwhile, 2-Mim (0.328 g) was dissolved in the same volume of methanol. Then, these two solutions were mixed and the mixed solution was stirred at 300 rpm for 2 h. After that, the mixed solution was stewed at ambient temperature for 24 h. The products were obtained and washed with methanol 3 times. Lastly, these yielded products were dried overnight at 60 °C in a vacuum. Fe/ZIF-8 containing various Fe contents is expressed as *x*% Fe-ZIF-8, where *x*% represents the inventory ratio of $Fe^{2+}/(Fe^{2+} + Zn^{2+})$.

For the preparation of DOX@7FZ nanoparticles, $Zn(NO_3)_2{\cdot}6H_2O$ and $FeSO_4{\cdot}7H_2O$ were added into 18.7 mL methanol and stirred for 5 min (Liquid A). Doxorubicin hydrochloride was dispersed in 1.3 mL of methanol ultrasonically (Liquid B). Next, Liquid B was slowly dropped into Liquid A and stirred for 2 min (Liquid C). 2-Mim was dissolved in 20 mL of methanol (Liquid D). Then Liquids C and D were mixed and aged for 24 h after stirring at ambient temperature for 2 h. The products were obtained and washed with methanol 3 times. Finally, these products were dried in a vacuum overnight at 60 °C.

X-ray diffraction (XRD), IR spectroscopy and X-ray photoelectron spectroscopy (XPS) were carried out on a Bruker SMART APEX diffractometer (λ = 0.71073 Å), a WQF-510A FT-IR spectrometer (Beijing Beifen-Ruili Analytical Instrument

Group Co., Ltd, China) and a Thermo ESCLALAB 250XI (Thermo, America), respectively. A Tristar II 3020 instrument (Micromeritics (Shanghai) Instrument Co., Ltd, China) was utilized to complete the nitrogen adsorption/desorption analysis. Both zeta potential and particle size were obtained from a W3895 of Microtrac Inc. (America). The external and internal morphologies of the products were observed using a scanning electron microscope (SEM, Regulus100 Hitachi, Japan) and a transmission electron microscope (TEM, FEI Tecnai G2 F20 FEI, America), respectively.

2.3. Drug release of DOX@7FZ

A typical drug releasing system was prepared using 10 mg DOX@7FZ powder which was suspended in 50 mL of PBS buffer (pH = 7.4, 6.4 and 5.3, respectively) at 37 °C. The prepared release system was placed on a thermostatic heating magnetic stirrer at 37 °C, 200 r min^{-1} 4 mL of the solution was taken at each time point and the corresponding volume of PBS buffer was added. The sample solution was centrifuged at a speed of 12 000 r min^{-1} for 5 min. A UV-visible spectrophotometer (UV-650, Shanghai mapada Instrument Co., Ltd, China) was employed to record the UV- visible spectra of the samples.

2.4. Cytotoxicity of DOX@7FZ *in vitro*

The cellular cytotoxicity of DOX@7FZ was determined by using the 3-(4, 5-dimethylthiazol-2-yl)-2,5-diphenyltetrazolium bromide (MTT) assay kit (Beyotime Biotechnology, Shanghai, China). To pre-culture, both MCF-7 cells and LO2 cells were cultured in 96 well plates (5×10^3 cells per well) and incubated in an incubator with 5% CO_2 at 37 °C for 24 h. After discarding the fluid in the well, 100 μL per well of the Dulbecco's Modified Eagle Medium (DMEM) with PBS and different concentrations of ZIF-8, 7FZ, DOX and DOX@7FZ were added. After 24 h, 10 μL of MTT (5 mg mL^{-1}) was added after discarding the fluid in the wells and incubated for another 4 h. Finally, a multifunctional microplate reader (Multiskan Sky ThermoFisher Co., Ltd, America) was used to detect the absorbance in each well. The results were expressed as the ratio of cell viability between the control group and experimental group.

2.5. Iron content detection

The intracellular iron content of MCF-7 cells was detected *via* the intracellular iron colorimetric assay kit (Applygen, Beijing, China). MCF-7 cells were cultured in twelve-well plates (5×10^5 cells per well) and incubated in an incubator for 24 h. To work out the relationship between the concentrations of nanoparticles and iron content, MCF-7 cells were treated as follows: PBS group (control group), ZIF-8 group, and 7FZ group at 5, 15, and 30 μg mL^{-1}. To observe the change of iron content in 24 h, MCF-7 cells were treated as follows: control group and DOX@7FZ group at 30 μg mL^{-1}. After treatments, these treated cells were collected and lysed with lysis buffer. The intracellular iron content was accurately measured, which is consistent with the directions provided in the kit.

2.6. *In vitro* ROS and MDA determination

The ROS content in cells was determined using a ROS fluorescence probe (dichloro-dihydro-fluorescein diacetate (DCFH-DA, Beyotime Biotechnology, Shanghai, China). MCF-7 cells were seeded in six-well plates (1×10^6 cells per well) and incubated for 24 h. The fluid from the wells was discarded, and the cells were treated as follows: control group, positive control group, and experimental group (30 μg mL^{-1}). Following incubation for 6 h, 0.1% DCFH-DA was added to each well and the cells were incubated for 30 min. Cells which were unresponsive to DCFH-DA were removed with PBS and observed under a fluorescence-inverted microscope (Olympus, Tokyo, Japan) as well as detected by flow cytometry (Accuri C6 Plus from BD Biosciences Co, Ltd, China).

The MDA assay kit (TBA method, Beyotime Biotechnology, Shanghai, China) was used to measure the intracellular levels of MDA. After treatment with PBS, ZIF-8, 7FZ, DOX and DOX@7FZ at a concentration of 30 μg mL^{-1}, MCF-7 cells were collected and counted. The intracellular content of MDA was determined according to the instructions provided in the kit.

2.7. Western blot analysis

The MCF-7 cells were cultured in 6 well plates and incubated for 24 h. After discarding the fluid from the plates, the complete medium containing PBS, ZIF-8, 7FZ, DOX and DOX@7FZ nanoparticles at 30 μg mL^{-1} was added into the plates again. Then, those treated MCF-7 cells were harvested and lysed with RIPA lysis buffer. The Bcl-2 and GPX-4 contents were both determined using western blot analysis.

2.8. *In vivo* therapeutic efficacy

A total of 25 female BALB/c nude mice were classified into 5 groups (PBS group, ZIF-8 group, 7FZ group, DOX group and DOX@7FZ group). 5×10^6 MCF-7 cells were injected into mice subcutaneously in the armpits at the age of 5 weeks. Three weeks after MCF-7 cell injection, mice were injected with 50 mg kg^{-1} agents (PBS, ZIF-8, 7FZ, DOX and DOX@7FZ) intravenously once a week for three weeks. One week after the last injection, mice were sacrificed by overdose anesthetic (pentobarbital sodium) for sample collection.

After anesthesia, the weight of nude mice was measured at first. Then the tumors as well as the major organs (heart, liver, spleen, lungs and kidneys) were both dissected. As for those dissected tumors, the long diameter and short diameter of tumors were measured. Then tumors and organs were fixed in 4% PFA overnight. After fixation, the tumors and organs were dehydrated and embedded in paraffin, and were cut in sequential sections systematically using a microtome (Leica, RM2016, Shanghai, China). Hematoxylin-eosin staining (H & E) was utilized to stain the sections after deparaffinization and rehydration. For immunofluorescence staining, sections were treated with 10% goat serum for 20 minutes to block non-specific protein adsorption. Next, sections were incubated with rabbit anti-Bcl2 (2 μg mL^{-1}, Cat No. PA5-20068 Invitrogen, USA) and rabbit anti-GPX4 antibody (1 : 100, PA5-120674, Invitrogen, USA)

at 4 °C overnight. Thereafter, they were washed with PBS three times and afterwards incubated with HRP-conjugated secondary antibodies (1 : 400, Cat no. 31466, Invitrogen, USA) for 30 min at room temperature while being protected from the light. DAPI was utilized for nuclei staining and these sections were observed and analyzed by using a confocal laser scanning microscope. All the major organs of nude mice were stained with H & E as well.

2.9. Statistical analysis

All experiments were repeated at least 3 times. The significance of the obtained data was assessed *via* a statistical method, one-way analysis of variance (ANOVA). The obtained digital results were expressed as the mean ± standard deviation. P values < 0.05 were denoted as statistical significance.

3. Results and discussion

3.1. Synthesis of iron-doped ZIF-8

Different ratio iron-doped ZIF-8 (denoted as x% Fe-ZIF-8, where x% represents the inventory ratio of $Fe^{2+}/(Fe^{2+} + Zn^{2+})$) particles were prepared at room temperature in methanol *via* a simple procedure reported previously.[46] The as-prepared materials were denoted as 5% Fe-ZIF-8 (5FZ), 7% Fe-ZIF-8 (7FZ) and 15% Fe-ZIF-8 (15FZ), respectively. In the FT-IR spectrum of the samples, the signal near 1077 cm^{-1} is ascribed to the C–N stretching of the imidazole unit, while the signal near 1582 cm^{-1} is related to the C=N stretching (Fig. S1, ESI†).[46,47] XRD was first utilized to explore the crystal structures of as-prepared x% Fe-ZIF-8 powders. As shown in Fig. 1B, the XRD patterns of these as-prepared materials are in good accordance with those of pure ZIF-8. Additionally, no new peaks appeared in the XRD patterns with the doping of Fe, implying that the Fe substituted Zn doping into ZIF-8 samples.[47] But, it is worth noting that the peak intensity of the XRD patterns was apparently lowered while the doping content was up to 15%, manifesting that there was no effect on the crystallization of x% Fe-ZIF-8 if the amount of doping Fe content was excessive. Next, to choose the appropriate particle to serve as a drug carrier, the effects of the zeta potential and size of x% Fe-ZIF-8 were determined (Fig. S2, ESI†). It was found that the zeta potential decreased gently while the ratio of doping Fe increased. In contrast, the sizes were increased while the ratio of doping Fe increased. Both of these obtained results demonstrated that the stability of Fe-doping ZIF-8 declined with the increase in the ratio of Fe doping. To reach the aim of the maximization of Fe content as well as retaining structure stability, 7FZ was chosen for further medical application.

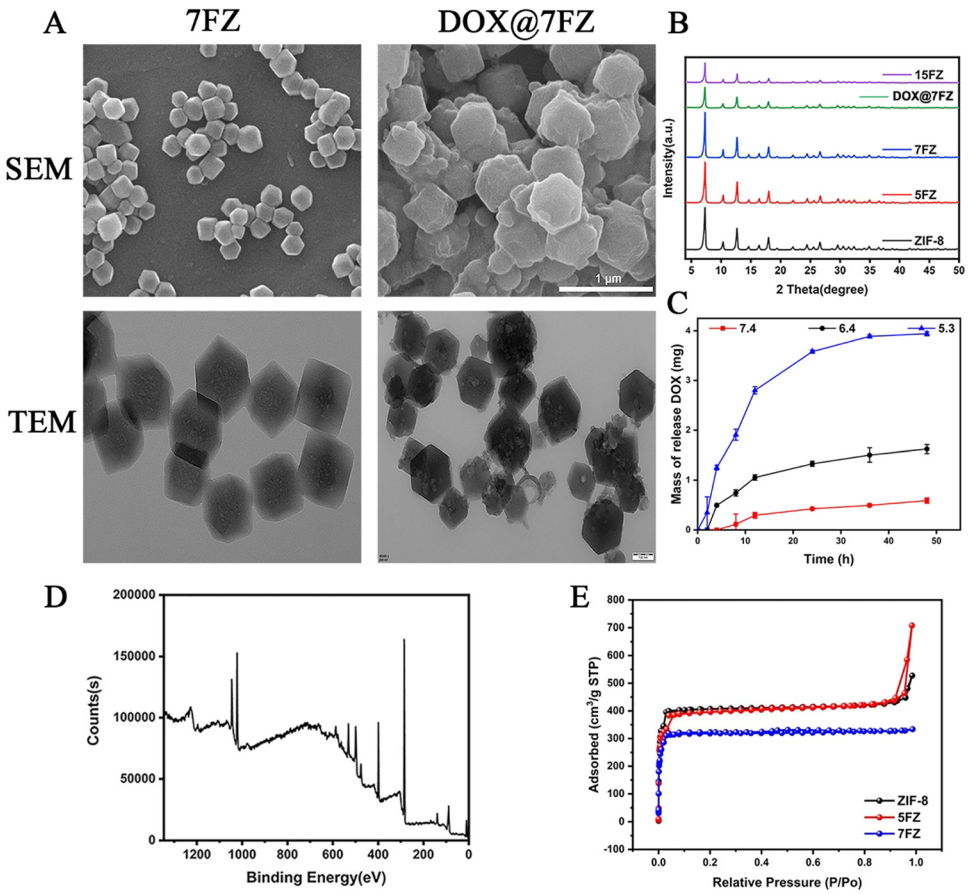

Fig. 1 (A) SEM and TEM images of 7FZ and DOX@7FZ nanocomplexes. (B) XRD patterns of nanoparticles. (C) *In vitro* release of DOX@7FZ nanocomplexes in pH 7.4, 6.4 and 5.3. (D) XPS wide scan spectra of DOX@7FZ. (E) Nitrogen adsorption–desorption isotherms of the as-synthesized ZIF-8, 5FZ and 7FZ.

3.2. Encapsulation of DOX in 7% Fe-ZIF-8 (7FZ)

X-Ray photoemission spectroscopy (XPS) was performed to analyze the elemental composition and atomic valence of 7FZ. Based on the results of XPS spectra (Fig. S3, ESI†), it is revealed that Zn, Fe, C, N and O co-exist in the structure of 7FZ, and a Fe–N_x peak is observed at 399.18 eV indicating the successful synthesis of 7FZ (Fig. S3, ESI†).[46] Moreover, five peaks were found by deconvoluting the XPS spectra of Fe2p (Fig. 1D), including the Fe(II) $2p^{1/2}$ peak at 725.98 eV, the Fe(III) $2p^{1/2}$ peak at 722.03 eV and the Fe(III)$2p^{3/2}$ peak at 712.13 eV (Table S1, ESI†), meaning that Fe exist as both Fe(II) and Fe(III) in the 7FZ.[48] As DOX is loaded into our materials by a one-step way, the color of the yields changed, from light yellow to purple (Fig. S4, ESI†). After the encapsulation of DOX, we first monitored the crystal phase of 7FZ by XRD. As shown in Fig. 1B, the DOX-loaded 7FZ (DOX@7FZ) particles remained highly crystalline with sharp diffraction peaks, but the peak intensity at low angles of 7FZ decreased due to the existence of DOX in the pores of 7FZ crystals. Moreover, diffraction peaks related to the DOX molecules were not observed in the resulting XRD pattern, implying that DOX crystals were non-existent in DOX@7FZ materials. Scanning electron microscopy (SEM) showed that the morphologies of DOX@7FZ particles are bumpy on the surface, but the octahedron structure which is the same as the 7FZ ones, indicating that the drug-loading process has a little impact on the 7FZ morphology (Fig. 1A). Meanwhile, transmission electron microscopy (TEM) showed that the size of mesopores grew bigger as well as inhomogeneous when loading DOX into 7FZ (Fig. 1A). The surface charge is crucial for the physical stability as well as redispersibility of nanoparticles, hence, we measure the zeta potentials of the as-synthesized particles.[49] It was found that the zeta potential of DOX@7FZ decreased to -4.45 ± 1.12 mV when it was compared to that of 7FZ (1.88 ± 0.51 mV). Afterward, the extural and porous properties of specific surface areas of ZIF-8, 5FZ and 7FZ were determined by nitrogen adsorption at 77 K (Fig. 1E). The Brunauer–Emmett–Teller (BET) surface areas of ZIF-8, 5FZ and 7FZ were measured to be 2302, 1271 and 1206 $m^2\ g^{-1}$ with the coexistence of micro- and mesoporous structures, which provided the nanocarrier with ideal drug loading properties (Table S2, ESI†).

After the verification of the successful synthesis of DOX@7FZ, the properties of drug release of the encapsulated DOX were investigated by UV-visible spectrophotometry. The loading efficacy was evaluated to be $58.01 \pm 0.02\%$. The release kinetics of DOX from DOX@7FZ under different pH conditions are shown in Fig. 1C. It can be observed virtually that the release behavior of DOX from the nanoparticles is pH-dependent. There was $67.94 \pm 0.72\%$ of DOX released from DOX@7FZ under acidic solutions (pH = 5.3) in 48 hours while only $10.19 \pm 0.93\%$ of DOX was released under physiological pH conditions (pH = 7.4) over the same period. This phenomenon is probably owing to the similar structure of 7FZ to pure ZIF-8 which has a characteristic of responding dissolution under acidic conditions (pH = 5–6). The imidazole bond is protonated after immersion in an acidic solution, and the acid-labile non-covalent bond between the metal ion and the imidazolium ion is destroyed, resulting in the structural degradation eventually.[50] Another potential reason for the acidic-responsive release of DOX@7FZ is that DOX exhibits a better hydrophilicity under acid solutions rather than neutral solutions.[51] There was only 67% drug released in 48 h at pH 5.3, which may be assigned to the more stable bonds between Fe^{3+} and DOX when compared to the bonds of Fe^{2+} and DOX.[51,52] Generally, there is no doubt that DOX@7FZ nanoparticles exhibit excellent pH-responsive capability, which aids in improving the delivery efficacy to the acidic tumor microenvironment obviously.

3.3. The level of iron in MCF-7 cells

The nanoparticles were engineered for inducing ferroptosis to improve the killing effect of DOX on breast cancer cells.[52] Therefore, the iron colorimetric assay was conducted to measure the total concentration of intracellular iron. We first quantified the concentration of iron in MCF-7 cells that were treated with the prepared frameworks without drug loading. The concentration of iron in breast cancer cells with 7FZ increased gradually with the increase of administration concentration (Fig. 2A). Meanwhile, the concentration of iron in MCF-7 cells administrated by 7FZ (92.39 ± 1.86 μM) was 1.66 times higher than with ZIF-8 (55.75 ± 2.77 μM) at a concentration of 30 μg mL^{-1}. As for the concentration of iron in MCF-7 cells treated with ZIF-8, it showed no difference to the control group with the increase of administration concentration, evidencing that the intracellular concentration of iron could be altered only when cells ingested the nanoparticles of 7FZ. Next, in order to explore the changes the DOX@7FZ brings out, we measured the concentration of iron in MCF-7 cells treated with DOX@7FZ at different times. As shown in Fig. 2B, it is obvious that the concentration of iron increases as time goes by and up to 48.15 ± 5.83 μM at 24 h, demonstrating that the drug loaded nanoparticles, DOX@7FZ, retain the ability of affecting iron balance in breast cancer cells. However, considering the chelation between iron ions and DOX, the release of iron from the framework (7FZ) might be slower, resulting in a lower concentration of iron in cells administrated by DOX@7FZ at 45 μg mL^{-1} than that by 7FZ at 30 μg mL^{-1} eventually.[53,54]

3.4. *In vitro* killing efficacy for MCF-7 cells

The cytotoxicity of DOX@7FZ on LO2 and MCF-7 cells was quantitively assessed by MTT assays at various concentrations. The MCF-7 cells were treated with different nanoparticles for 24 h and the untreated cells were taken as a control. As shown in Fig. 3A, the viability of treated MCF-7 descended with increased DOX@7FZ concentrations. Specifically, the cytotoxicity of DOX@7FZ below 45 μg mL^{-1} was low but increased evidently while the concentrations were over 45 μg mL^{-1}. The cell viabilities of DOX@7FZ were 51.58% and 13.98%, corresponding to a concentration of 45 μg mL^{-1} and 60 μg mL^{-1}. Meanwhile, it is worth noting that no significant decrease in the toxicity of free DOX was observed under various concentrations for 24 h, on account of which DOX is a time-dependent chemotherapy drug.[55] In summary, DOX@7FZ, as a nanocarrier for DOX, could shorter the onset of action for DOX. For comparison, after 24 h of coincubation with different nanoparticles

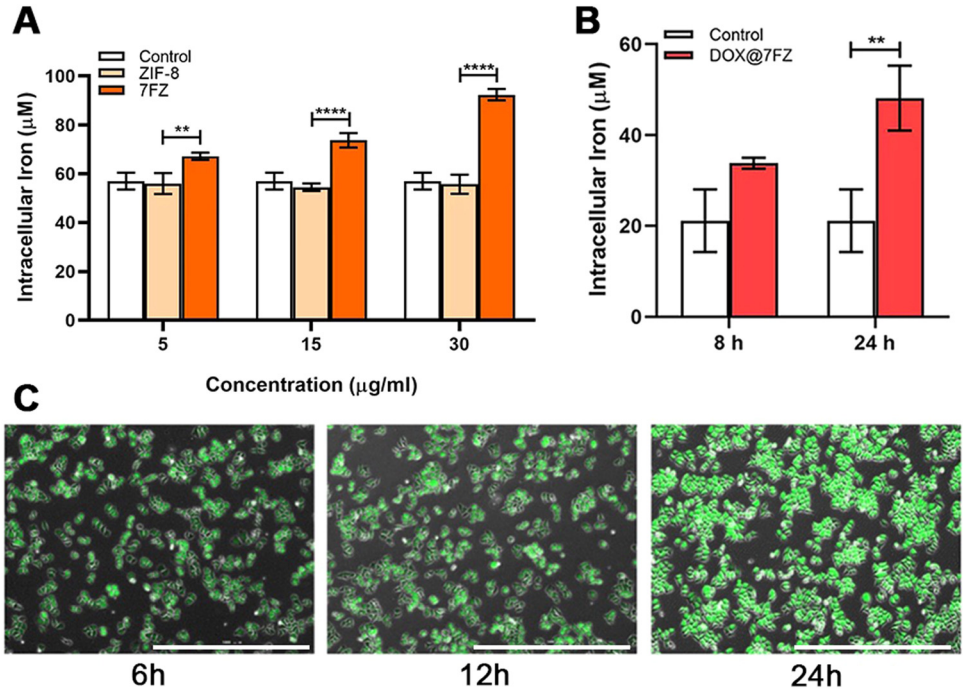

Fig. 2 (A) The concentrations of intracellular iron in MCF-7 cells treated with ZIF-8 and 7FZ nanoparticles in 5, 15 and 30 μg mL^{-1}. (B) The changes of concentrations of intracellular iron in MCF-7 cells treated with DOX@7FZ at 30 μg mL^{-1} for 24 h. (C) Image of intracellular change of ROS in 24 h.

below the concentration of 60 μg mL^{-1}, it was obviously observed that DOX@7FZ manifested rather less cytotoxicity on LO2 cells compared with free DOX, which could be attributed to the ability of acidic-responsive release of DOX@7FZ in the tumor microenvironment instead of normal tissues (Fig. 3B). However, the cell viability of LO2 treated with DOX@7FZ decreased sharply to 13.35% at a concentration of 60 μg mL^{-1}. This is mainly because the iron ions released from DOX@7FZ over accumulated in LO2 cells, leading to the imbalance of iron homeostasis.[56] On no account, it could be anticipated that the lower toxicity of DOX@7FZ against LO2 would mitigate its side effect to normal organs, highlighting the innate virtue of passive targeting nanocarriers, to some extent. The above results suggest that the premade DOX@7FZ is capable of serving as an actively targeted nanocarrier to enhance the efficacy of chemotherapy. Referring to the obtained results, the following experiments for determining the mechanism of DOX@7FZ will be conducted at a concentration of 45 μg mL^{-1}.

3.5. The level of ROS in MCF-7 cells

Iron accumulation and lipid peroxidation are both characteristics of ferroptosis, thence we measured the level of lipid hydroperoxides by the thiobarbituric acid (TBA) assay using UV/visible spectrophotometry as well.[57–59] According to the reported studies, DOX is capable of causing an increased production of ROS, including the products of lipid peroxidation, and the result we attained indeed showed that the level of lipid hydroperoxides in breast cancer cells treated with DOX was higher than in the

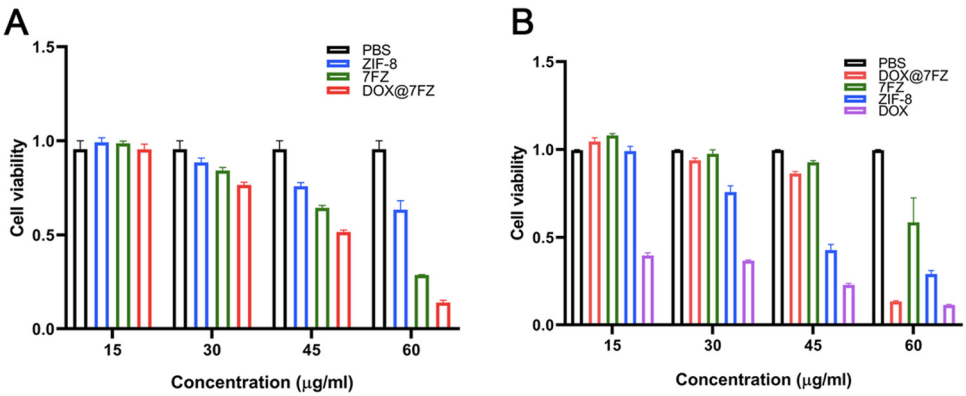

Fig. 3 (A) Cell viability of MCF-7 cells treated with PBS, ZIF-8, 7FZ and DOX@7FZ at different concentrations. (B) Cell viability of LO2 treated with PBS, ZIF-8, 7FZ, DOX and DOX@7FZ at different concentrations.

control group (Fig. 4A).[60,61] After encapsulating DOX, DOX@7FZ made breast cancer cells produce more lipid hydroperoxides than the single DOX did, implying that DOX@7FZ has a better ability of enhancing the level of lipid peroxidation in breast cancer cells overall.

Despite measuring the yields of lipid peroxidation, we examined the concentration of integrated ROS in breast cancer cells at the same time. The data illustrated that the intracellular fluorescence intensity increased distinctly while MCF-7 cells incubated with DOX@7FZ at a concentration of 45 μg mL^{-1}. It is worth noting that the fluorescence intensity detected in the ZIF-8 group was lower than that detected in the control group at the same concentration (Fig. 4B). The main reasons for this result are that zinc in ZIF-8 plays an important role in the stabilization of membranes by inhibiting NADPH-oxidase, and it is also a component of SOD, an excellent free radical scavenger in our bodies.[62] The fluorescence images shown in Fig. 2Cshow intuitively that the DOX@7FZ is capable of enhancing the level of ROS in MCF-7 cells time-dependently, which is the same as the change of iron concentration in MCF-7 cells.

3.6. The possible mechanism of DOX@7FZ

As for further investigating the therapeutic mechanism of DOX@7FZ, the expression of key ferroptosis and apoptosis proteins including GPX-4, Bcl-2 and NOX-4 in MCF-7 cells was measured by western blot analysis.[63,64] GPX4, utilizing GSH as its cofactor to maintain the integrity of biomembranes by detoxifying LPO, is the main negative regulator of ferroptosis.[65] Thence, the expression level of GPX4 and the activity of ferroptosis are inversely related. In preliminary experiments we found that the GPX4 level in MCF-7 cells treated with DOX@7FZ was down-regulated sharply and it has decreased by 3.3-fold compared with that observed with single DOX treatment. (Fig. S5 and S9, ESI†) The results demonstrated that there existed a strong down-regulation on GPX4 in the cooperation of released iron ions and DOX. The data well agree with the results of iron concentration in MCF-7 cells treated with DOX@7FZ. Moreover, as depicted in Fig. 4C and Fig. S8 (ESI†), the expression of GPX4 decreased sharply at first 6 h in comparison to those of other two proteins, which implies that it is probable that DOX@7FZ will make an influence on the level of ferroptosis-related ROS by releasing Fe(II)/Fe(III) ions in MCF-7 cells firstly.

Moreover, the apoptosis-associated protein Bcl-2 was also detected. Bcl-2, an anti-apoptosis protein, is a critical regulator in the molecular mechanism of apoptosis.[66] As for Bcl-2, the single DOX and DOX@7FZ groups showed elevated Bcl-2 levels, and the level of Bcl-2 in MCF-7 cells in the DOX@7FZ group was

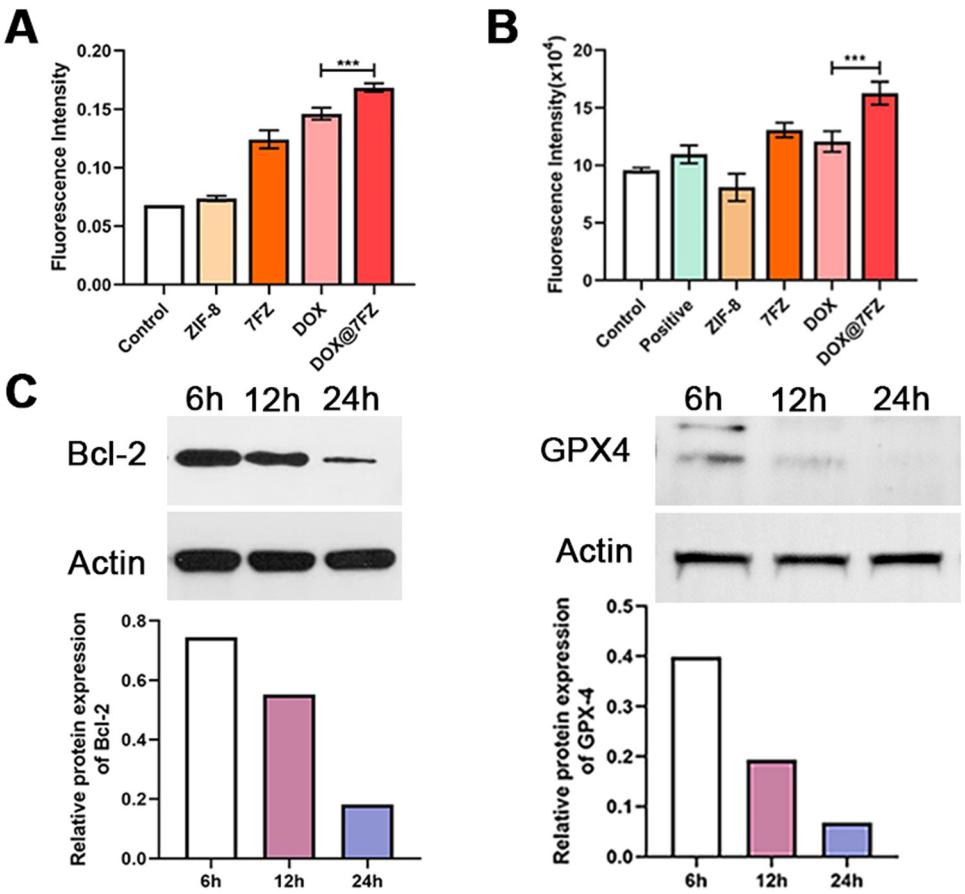

Fig. 4 (A) MDA levels of MCF-7 cells treated with ZIF-8, 7FZ, DOX and DOX@7FZ. The DOX concentration was set at 7 μg mL^{-1}. (B) Flow cytometric results of DCFH-DA in MCF-7 cells treated with ZIF-8, 7FZ, DOX and DOX@7FZ. The DOX concentration was set at 7 μg mL^{-1}. (C) Western blot analysis and the matching quantitative data of Bcl-2 and GPX4 in MCF-7 cells with various treatments as indicated. β-actin (denoted as Actin) was set as a control.

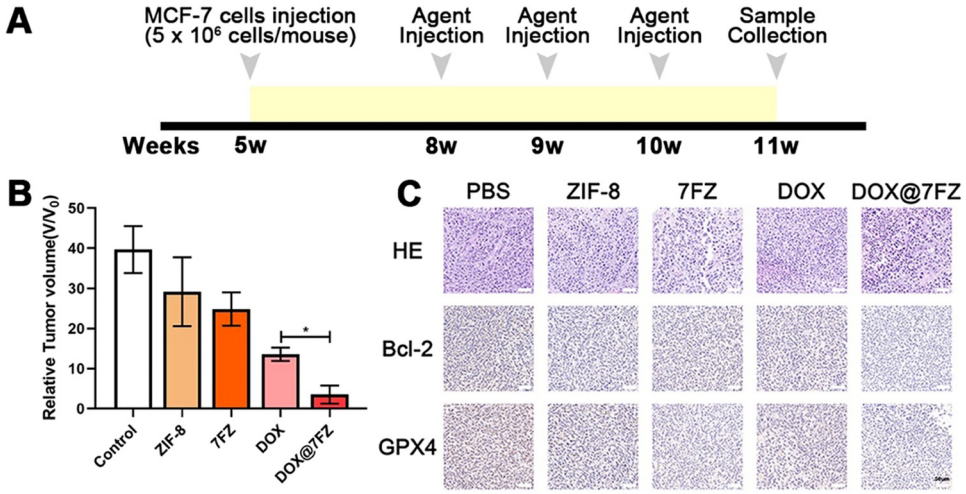

Fig. 5 (A) Schematic illustration of MCF-7 tumor-bearing mice model in cancer therapy. (B) Relative tumor volume of mice groups after treatment with PBS, ZIF-8, 7FZ, DOX and DOX@7FZ. (C) H & E staining of tumors and immunohistochemical staining of Bcl-2 and GPX4 in various mice groups. Scale bar: 50 μm.

1.4-fold lower than in the single DOX group, implying that the combination of iron ions and DOX is capable of promoting the progression of apoptosis (Fig. S5 and S9, ESI†). With time increasing, the expression of Bcl-2 decreased gradually, and reached the minimum level at 24 h. (Fig. 4C and Fig. S7, ESI†) The attained results revealed that apoptosis might be activated with the release of DOX from DOX@7FZ and accelerated by the increasing level of ROS produced by ferroptosis.

3.7. *In vivo* anticancer efficacy and the safety of DOX@7FZ

The anticancer efficacy *in vivo* was evaluated by using MCF-7 tumor bearing mice. Tumor-bearing mice were randomly divided into five groups (n = 5) of PBS (control group), ZIF-8, 7FZ, DOX, and DOX@7FZ. On weeks 8, 9 and 10, equivalent DOX (50 mg kg^{-1}) and the other nanoparticles (5 mg kg^{-1}) were injected intravenously into the mice (Fig. 5A). The weight of nude mice, and the long diameter and short diameter of tumor were

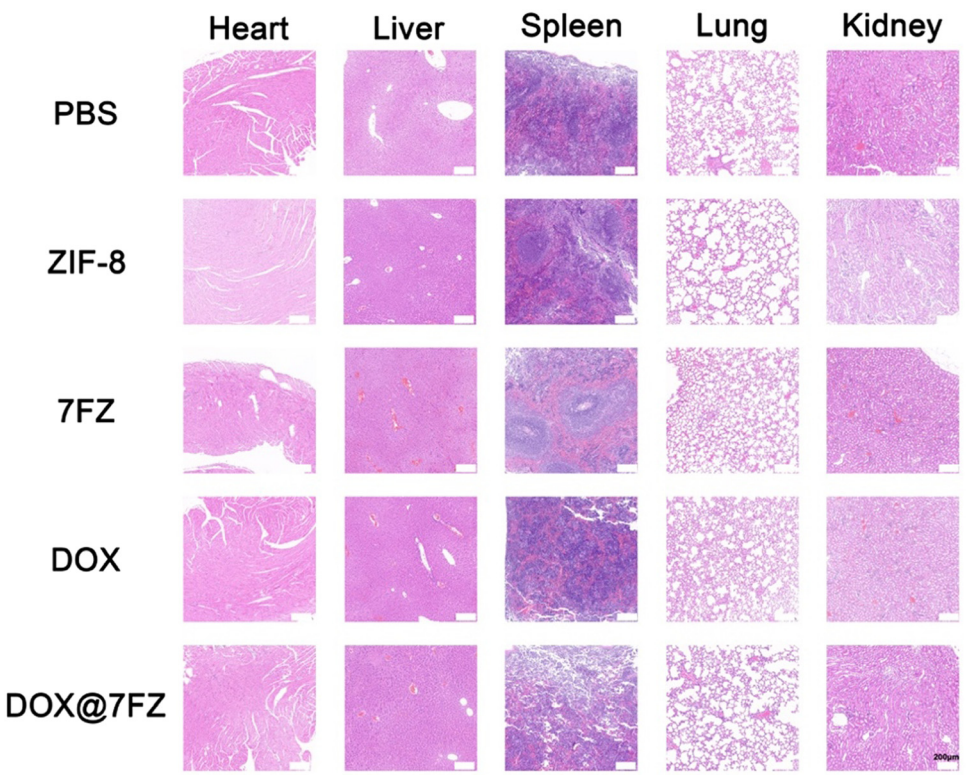

Fig. 6 H & E staining images of organs from various mice groups. Scale bar: 200 μm.

measured. The tumor volume was calculated (tumor volume = long diameter × short diameter^2). The weights of mice of the PBS group, ZIF-8 group, 7FZ group, DOX group and DOX@7FZ group were 22.75 ± 2.11 g, 22.03 ± 0.5 g, 21.99 ± 1.82 g, 21.91 ± 1.75 g and 21.44 ± 0.7 g, respectively. There was no significant difference in the body weight of mice among all the groups. The tumor volume of the DOX@7FZ group was 3.3 ± 2.02 mm^3. Compared with that of the PBS group (42.91 ± 6.97 mm^3) and DOX group (13.58 ± 1.50 mm^3), the tumor volume of the DOX@7FZ group was significantly smaller (Fig. 5B and Fig. S6, ESI†).

To further clarify the pathological characteristics of the tumor, hematoxylin and eosin (H & E) staining was performed on the tumor tissue. In the PBS group, the cell morphology was intact (Fig. 5C). In the DOX group and the DOX@7FZ group, large areas of shrunken cells with condensed cytoplasm and pyknotic and fragmented nuclei were observed (Fig. 5C). No inflammation was seen in the DOX@7FZ group. The results demonstrated that the cancer cells in the DOX@7FZ group underwent programmed cell death rather than cell necrosis. Immunohistochemical staining of Bcl-2 and GPX-4 was further performed. Compared with the PBS group, the levels of both Bcl-2 protein and GPX-4 protein were down-regulated in the DOX@7FZ group. The degree of down-regulation of Bcl-2 and GPX-4 in the DOX@7FZ group was obviously higher than that in the single DOX and 7FZ groups. Including the results of western blot, all the results suggested that DOX@7FZ could initiate apoptosis and induce ferroptosis, leading to programmed cell death.

To assess the biocompatibility of DOX@7FZ *in vivo*, all mice were sacrificed after the animal models were established. H & E staining was performed on the major organs. There was no significant difference in the heart, liver, spleen, lungs and kidneys among all the groups, and no obvious lesion was observed (Fig. 6). The results only showed that DOX@7FZ had good biological tolerance in living bodies.

4. Conclusion

In summary, we have designed a ferrous-supply nanocarrier for DOX employing the self-assembly of DOX, 2-MIM and $FeSO_4$, which is a facile one-pot method. Among the components of the carrier, the doping of iron ions facilitated the performance of the synergetic effect of ferroptosis and apoptosis. Thence, DOX@7FZ was identified to have a marked ability on promoting the apoptosis and enhancing the level of intracellular oxidative stress strongly with a octahedron structure. The increasing oxidative stress further led to the ferroptosis in tumor cells. Consequently, an effective antitumor performance was exhibited under the combination of apoptosis and ferroptosis. The strategy of combination therapy between apoptosis and ferroptosis has great potential to furnish wise insights into devising more efficient chemotherapy plans for antitumor treatment in the future.

Statement

All animal experiments of this study were performed under the National Institutes of Health Guidelines on the Use of Laboratory Animals, then were approved by the Institute's Animal Ethics Committee of Shanghai Ninth People's Hospital, Shanghai Jiao Tong University School of Medicine (SH9H-2023-A298-SB).

Conflicts of interest

The authors have no conflicts of interest with the contents of this article.

Acknowledgements

This research was also partially funded by the Key Scientific Research Project of Colleges and Universities of Education Department of Guangdong Province (20202ZDZX2046 and 2021ZDZX2052, 2022ZDZX2022), the Guangdong Basic and Applied Basic Research Foundation (2021A1515011616), the Guangdong Medical University Research Project (1019k2022003), the open research fund of Songshan Lake Materials Laboratory (2022SLABFN12), the Natural Science Foundation of Guangdong Province (2023A1515011536), the Featured Innovation Project of Guangdong Province (2022KTSCX045), the Guangdong Provincial Medical Science and Technology Research Fund project (A2023484), the Dongguan Social Development Science and Technology Project (no. 20211800904802) and the Science and technology project of Zhanjiang City (no. 2021B01448). Dr Mohd. Muddassir is grateful to Researchers Supporting Project number (RSP2023R141), King Saud University, Riyadh, Saudi Arabia, for financial assistance. Dr Y. Pan thanks the China Scholarship Council (202108440263).

References

1 https://www.iarc.who.int/cancer-type/breast-cancer/.
2 L. A. Korde, M. R. Somerfield, L. A. Carey, J. R. Crews, N. Denduluri, E. S. Hwang, S. A. Khan, S. Loibl, E. A. Morris, A. Perez, M. M. Regan, P. A. Spears, P. K. Sudheendra, W. F. Symmans, R. L. Yung, B. E. Harvey and D. L. Hershman, *J. Clin. Oncol.*, 2021, **39**, 1485–1505.
3 W. J. Gradishar, B. O. Anderson, J. Abraham, R. Aft, D. Agnese, K. H. Allison, S. L. Blair, H. J. Burstein, C. Dang, A. D. Elias, S. H. Giordano, M. P. Goetz, L. J. Goldstein, S. J. Isakoff, J. Krishnamurthy, J. Lyons, P. K. Marcom, J. Matro, I. A. Mayer, M. S. Moran, J. Mortimer, R. M. O' Regan, S. A. Patel, L. J. Pierce, H. S. Rugo, A. Sitapati, K. L. Smith, M. L. Smith, H. Soliman, E. M. Stringer-Reasor, M. L. Telli, J. H. Ward, J. S. Young, J. L. Burns and R. Kumar, *J. Natl. Compr. Canc. Netw.*, 2020, **18**, 452–478.
4 L. Biganzoli, N. M. L. Battisti, H. Wildiers, A. McCartney, G. Colloca, I. H. Kunkler, M. J. Cardoso, K. L. Cheung, N. A. de Glas, R. M. Trimboli, B. Korc-Grodzicki, E. Soto-Perez-de-Celis, A. Ponti, J. Tsang, L. Marotti, K. Benn, M. S. Aapro and E. G. C. Brain, *Lancet Oncol.*, 2021, **22**, e327–e340.
5 M. A. Franzoi, E. Agostinetto, M. Perachino, L. Del Mastro, E. de Azambuja, I. Vaz-Luis, A. H. Partridge and M. Lambertini, *Lancet Oncol.*, 2021, **22**, e303–e313.

6 G. Q. Wei, Y. Wang, G. Yang, Y. Wang and R. Ju, *Theranostics*, 2021, **11**, 6370–6392.
7 (*a*) E. C. Cheung and K. H. Vousden, *Nat. Rev. Cancer*, 2022, **22**, 280–297; (*b*) W. P. Chen, M. Liu, H. P. Yang, A. Nezamzadeh-Ejhieh, C. Y. Lu, Y. Pan, J. Q. Liu and Z. Bai, *Pharmaceutics*, 2023, **15**, 1323; (*c*) X. L. Chen, M. M. Li, M. Z. Lin, C. Y. Lu, A. Kumar, Y. Pan, J. Q. Liu and Y. Q. Peng, *J. Mater. Chem. B*, 2023, DOI: **10.1039/D3TB00267E**; (*d*) B. Ogretmen, *Nat. Rev. Cancer*, 2018, **18**, 33–50; (*e*) M. M. Li, S. H. Yin, M. Z. Lin, X. L. Chen, Y. Pan, Y. Q. Peng, J. B. Sun, A. Kumar and J. Q. Liu, *J. Mater. Chem. B*, 2022, **10**, 5105–5128.
8 (*a*) M. D. Brand, *Exp. Gerontol.*, 2010, **45**, 466–472; (*b*) J. Y. Chen, Z. X. Zhang, J. X. Ma, A. Nezamzadeh-Ejhieh, C. Y. Lu, Y. Pana, J. Q. Liu and Z. Bai, *Dalton Trans.*, 2023, **52**, 6226–6238.
9 (*a*) M. P. Murphy, *Biochem. J.*, 2019, **417**, 1–13; (*b*) Z. J. Xu, Z. Y. Wu, S. Huang, K. H. Ye, Y. H. Jiang, J. Q. Liu, J. C. Liu, X. W. Lu and B. Li, *J. Controlled Release*, 2023, **354**, 615–625; (*c*) W. C. Liu, Q. W. Yan, C. Xia, X. X. Wang, A. Kumar, Y. Wang, Y. W. Liu, Y. Pan and J. Q. Liu, *J. Mater. Chem. B*, 2021, **9**, 4459–4474.
10 T. Xu, S. J. Zhao, C. W. Lin, X. L. Zheng and M. H. Lan, *Nano Res.*, 2020, **13**, 2898–2908.
11 S. Kwiatkowski, B. Knap, D. Przystupski, J. Saczko, E. Kędzierska, K. Knap-Czop, J. Kotlińska, O. Michel, K. Kotowski and J. Kulbacka, *Biomed. Pharmacother.*, 2018, **106**, 1098–1107.
12 (*a*) Z. M. Tang, Y. Y. Liu, M. Y. He and W. H. Bu, *Angew. Chem. Int. Ed. Engl.*, 2019, **58**, 946–956; (*b*) Y. Lin, X. W. Chen, C. C. Yu, G. X. Xu, X. X. Nie, Y. F. Cheng, X. X. Luan and Q. X. Song, *Acta Biomater.*, 2023, **159**, 300–311.
13 (*a*) S. J. Dixon, K. M. Lemberg, M. R. Lamprecht, R. Skouta, E. M. Zaitsev, C. E. Gleason, D. N. Patel, A. J. Bauer, A. M. Cantley and W. S. Yang, *Cell*, 2012, **149**, 1060–1072; (*b*) H. L. Yu, J. Q. Yan, Z. P. Li, T. T. Song, F. Ning, J. S. Tan and Y. Sun, *Mater. Chem. B*, 2023, **11**, 415–429.
14 B. R. Stockwell, J. P. F. Angeli, H. Bayir, A. I. Bush, M. Conrad, S. J. Dixon, S. Fulda, S. Gascón, S. K. Hatzios and V. E. Kagan, *Cell*, 2017, **171**, 273–285.
15 D. L. Tang, X. Chen, R. Kang and G. Kroemer, *Cell Res.*, 2021, **31**, 107–125.
16 S. J. Dixon and B. R. Stockwell, *Ann. Rev. Cancer. Biol.*, 2019, **3**, 35–54.
17 J. A. Harrigan, X. Jacq, N. M. Martin and S. P. Jackson, *Nat. Rev. Drug Discovery*, 2018, **17**, 57–77.
18 S. Mumbauer, J. Pascual, I. Kolotuev and F. Hamaratoglu, *PLoS Genet.*, 2020, **16**, e1009138.
19 M. H. Gao, P. Monian, Q. H. Pan, W. Zhang, J. Xiang and X. J. Jiang, *Cell Res.*, 2016, **26**, 1021–1032.
20 B. Hassannia, P. Vandenabeele and T. V. Berghe, *Cancer Cell*, 2019, **35**, 830–849.
21 F. Cardoso, N. Harbeck, L. Fallowfield, S. Kyriakides and E. Senkus, *Annals Oncology*, 2012, **23**, vii11–vii19.
22 S. Bandarra, P. Cipriano, J. Goncalves, A. C. Ribeiro and I. Barahona, *Ann. Med.*, 2018, **50**, S25–S26.
23 G. Minotti, P. Menna, E. Salvatorelli, G. Cairo and L. Gianni, *Pharmacol. Rev.*, 2004, **56**, 185–229.
24 P. Singal and N. Iliskovic, *N. Engl. J. Med.*, 1998, **339**, 900–905.
25 Y. Lan, Q. W. Liang, Y. Sun, A. C. Cao, L. Liu, S. Y. Yu, L. Y. Zhou, J. X. Liu, R. Y. Zhu and Y. H. Liu, *ACS Appl. Mater. Interfaces*, 2020, **12**, 31904–31921.
26 Y. Y. Wen, X. Chen, X. F. Zhu, Y. C. Gong, G. L. Yuan, X. Y. Qin and J. Liu, *ACS Appl. Mater. Interfaces*, 2019, **11**, 43393–43408.
27 K. Chen, H. Cai, H. Zhang, H. Y. Zhu, Z. W. Gu, Q. Y. Gong and K. Luo, *Acta Biomater.*, 2019, **84**, 339–355.
28 Y. X. Yang, B. J. Sun, S. Y. Zuo, X. M. Li, S. Zhou, L. X. Li, C. Luo, H. Z. Liu, M. S. Cheng, Y. J. Wang, S. J. Wang, Z. G. He and J. Sun, *Sci. Adv.*, 2020, **6**, eabc1725.
29 U. Kanwal, N. Irfan Bukhari, M. Ovais, N. Abass, K. Hussain and A. Raza, *J. Drug Target*, 2018, **26**, 296–310.
30 H. Z. Zheng, J. Jiang, S. J. Xu, W. Liu, Q. Q. Xie, X. M. Cai, J. Zhang, S. J. Liu and R. B. Li, *Nanoscale*, 2021, **13**, 2266–2285.
31 Y. Qin, F. Tong, W. Zhang, Y. Zhou, S. Q. He, R. Xie, T. Lei, Y. S. Wang, S. J. Peng, Z. F. Li, J. L. Leong, H. L. Gao and L. G. Lu, *Adv. Funct. Mater.*, 2021, **31**, 2104645.
32 Y. C. Chu, T. Sun and C. Jiang, *Chin. Chem. Lett.*, 2022, **33**, 4157–4168.
33 L. Gao, J. Zhuang, L. Nie, J. Zhang, Y. Zhang, N. Gu, T. Wang, J. Feng, D. Yang, S. Perrett and X. Yan, *Nat. Nanotechnol.*, 2007, **2**, 577–583.
34 Z. J. Xu, Z. Y. Wu, S. Huang, K. H. Ye, Y. H. Jiang, J. Q. Liu, J. C. Liu, X. W. Lu and B. Li, *J. Controlled Release*, 2023, **354**, 615–625.
35 X. B. Ma, H. Y. Sui, Q. Yu, J. W. Cui and J. C. Hao, *Langmuir*, 2021, **37**, 3166–3172.
36 K. Liang, J. J. Richardson, J. Cui, F. Caruso, C. J. Doonan and P. Falcaro, *Adv. Mater.*, 2016, **28**, 7910–7914.
37 K. D. Lu, T. Aung, N. N. Guo, R. Weichselbaum and W. B. Lin, *Adv. Mater.*, 2018, **30**, 1707634.
38 M. Hu, Y. Ju, K. Liang, T. Suma, J. W. Cui and F. Caruso, *Adv. Func. Mater.*, 2016, **26**, 5827–5834.
39 Z. Zhang, W. Sang, L. S. Xie and Y. L. Dai, *Coord. Chem. Rev.*, 2019, **399**, 213022.
40 J. Liu, Q. X. Wen, B. Z. Zhou, C. N. Yuan, S. B. Du, L. Li, L. Y. Jiang, S. Q. Yao and J. Y. Ge, *ACS Chem. Biol.*, 2022, **17**, 32–38.
41 Q. S. Wang, Y. Sun, S. F. Li, P. P. Zhang and Q. Q. Yao, *RSC Adv.*, 2020, **10**, 37600–37620.
42 Y. T. Qin, H. Peng, X. W. He, W. Y. Li and Y. K. Zhang, *ACS Appl. Mater. Interfaces*, 2019, **11**, 34268–34281.
43 R. Li, X. Q. Ren, X. F. Feng, X. G. Li, C. W. Hu and B. Wang, *Chem. Commun.*, 2014, **50**, 6894–6897.
44 D. Saliba, M. Ammar, M. Rammal, M. Al-Ghoul and M. Hmadeh, *J. Am. Chem. Soc.*, 2018, **140**, 1812–1823.
45 Y. J. Deng, Y. Y. Dong, G. H. Wang, K. L. Sun, X. D. Shi, L. Zheng, X. H. Li and S. J. Liao, *ACS Appl. Mater. Interfaces*, 2017, **9**, 9699–9709.
46 G. Y. Ye, K. M. Zhao, Z. He, R. J. Huang, Y. C. Liu and S. Q. Liu, *ACS Sustainable Chem. Eng.*, 2018, **6**, 15624–15633.

47 L. H. Hu, L. Chen, X. Peng, J. W. Zhang, X. H. Mo, Y. J. Liu and Z. C. Yan, *Micropor Mesopor Mat.*, 2020, **299**, 110123.
48 H. Chen, Z. L. Yan, S. J. Wu and F. Li, *Colloids Surf., B*, 2021, **205**, 111902.
49 A. K. Jain and S. Thareja, *Artif Cell Nanomed B*, 2019, **47**, 524–539.
50 C. C. Zheng, Y. Wang, S. Z. F. Phua, W. Q. Lim and Y. L. Zhao, *ACS Biomater. Sci. Eng.*, 2017, **3**, 2223–2229.
51 S. G. Wang, Y. L. Wu, R. Guo, Y. P. Huang, S. H. Wen, M. W. Shen, J. H. Wang and X. Y. Shi, *Langmuir*, 2013, **29**, 5030–5036.
52 H. Amawi, H. M. Sim, A. K. Tiwari, S. V. Ambudkar and S. Shukla, *Adv. Exp. Med. Biol.*, 2019, **1141**, 549–580.
53 P. A. Janne, J. C. H. Yang, D. W. Kim, D. Planchard, Y. Ohe, S. S. Ramalingam, M. J. Ahn, S. W. Kim, W. C. Su, L. Horn, D. Haggstrom, E. Felip, J. H. Kim, P. Frewer, M. Cantarini, K. H. Brown, P. A. Dickinson, S. Ghiorghiu and M. Ranson, *N. Engl. J. Med.*, 2015, **372**, 1689–1699.
54 X. J. Liang, *Sci. China Mater.*, 2020, **63**, 2086–2088.
55 N. Pilco-Fereto and G. M. Calaf, *Int. J. Oncol.*, 2016, **49**, 753–762.
56 J. G. Bieri, *Nature*, 1959, **184**, 1148–1149.
57 J. Li, F. Cao, H. L. Yin, Z. J. Huang, N. Mao, B. Sun and G. Wang, *Cell Death Dis.*, 2020, **11**, 88.
58 H. J. Xu, D. Ye, M. L. Ren, H. Y. Zhang and F. Bi, *Trends Mol. Med.*, 2021, **27**, 856–867.
59 J. Bi, T.-A. Ichu, C. Zanca, H. Yang, W. Zhang, Y. Gu, S. Chowdhry, A. Reed, S. Ikegami, K. M. Turner, W. Zhang, G. R. Villa, S. Wu, O. Quehenberger, W. H. Yong, H. I. Kornblum, J. N. Rich, T. F. Cloughesy, W. K. Cavenee, F. B. Furnari, B. F. Cravatt and P. S. Mischel, *Cell Metab.*, 2019, **30**(3), 525–538.
60 S. Wang, E. A. Konorev, S. Kotamraju, J. Joseph, S. Kalivendi and B. Kalyanaraman, *J. Biol. Chem.*, 2004, **279**, 25535–25543.
61 J. N. Moloney and T. G. Cotter, *Sem. Cell Dev. Biol.*, 2018, **80**, 50–64.
62 D. D. Marreiro, K. J. C. Cruz, J. B. S. Morais, J. B. S. Beserra, J. B. Severo and A. R. S. De Oliveira, *Antioxidants*, 2017, **6**, 24.
63 Y. Xie, W. Hou, X. Song, Y. Yu, J. Huang, X. Sun, R. Kang and D. Tang, *Cell Death Differ.*, 2016, **23**, 369–379.
64 J. C. Reed, *Trends Mol. Med.*, 2001, **7**, 314–319.
65 G. Lei, C. Mao, Y. L. Yan, L. Zhuang and B. Y. Gan, *Protein Cell*, 2021, **12**, 836–857.
66 J. E. Chipuk, T. Moldoveanu, F. Llambi, M. J. Parsons and D. R. Green, *Mol. Cell*, 2010, **37**, 299–310.